Author/s:
Agheshlui, H;Sedaghat, MH;Matthai, S

Title:
Stress Influence on Fracture Aperture and Permeability of Fragmented Rocks

Date:
2018-05-01

Citation:
Agheshlui, H., Sedaghat, M. H. & Matthai, S. (2018). Stress Influence on Fracture Aperture and Permeability of Fragmented Rocks. Journal of Geophysical Research Solid Earth, 123 (5), pp.3578-3592. https://doi.org/10.1029/2017JB015365.

Agheshlui Hossein (Orcid ID: 0000-0002-8016-099X)
Matthäi Stephan, K. (Orcid ID: 0000-0001-7470-8026)

Stress Influence on Fracture Aperture and Permeability of Fragmented Rocks

Hossein Agheshlui[1], Mohammad H. Sedaghat[1], Stephan Matthai[1]

[1] Peter Cook Centre for CCS, Department of Infrastructure Engineering, The University of Melbourne, Parkville, Vic 3010, Australia

Corresponding author: Hossein Agheshlui (hossein.agheshlui@unimelb.edu.au)

Key Points:

- Fracture aperture computed from local (deviatoric stresses) as opposed to far-field stress; block rotations and displacements are considered.
- Three-dimensional modelling considering interaction between plastic and brittle layers.
- Equivalent permeability calculated considering complex stress states and aperture variations in individual fracture segments.

This is the author manuscript accepted for publication and has undergone full peer review but has not been through the copyediting, typesetting, pagination and proofreading process, which may lead to differences between this version and the Version of Record. Please cite this article as doi: 10.1029/2017JB015365

Abstract

The influence of far-field stresses on fracture apertures in a fragmented rock layer is investigated using finite element analysis of a three dimensional mechanical model. The model implements realistic boundary conditions, interactions between the fragmented layer and neighbouring plastic rock layers, and frictional interfaces between the rock blocks. Stress-strain analysis is conducted to obtain stress variations within the fragmented rock layer and the block displacements and rotations. The fracture apertures are calculated using the local stress states instead of the far-field stresses simply being projected on the fractures. It is observed that fracture apertures can vary for the fracture segments over the individual blocks. Ensemble permeability is calculated by running a single phase flow analysis considering the obtained fracture apertures for fracture segments. The influence of the rock block displacements, rotations and deformations, difference between the mechanical properties of the rock layers, and the orientation of the horizontal stresses is investigated on the ensemble permeability. It is demonstrated that the compressibility of the neighbouring layers and block rotations and deformations have significant influence on the permeability of the fragmented rock layer. These effects which may be ignored in simpler aperture calculation models can result in considerable inaccuracies in the estimation of fracture apertures and ensemble permeability. Hence, such methods may only be used as indicative tools.

Keywords: Fragmented rocks, fracture aperture, permeability tensor, frictional interface, in situ stress orientation

1 Introduction

The hydraulic properties of rock fractures are of considerable interest in several areas of engineering, such as petroleum and geothermal reservoirs (Kazemi & Gilman, 1993), mining (Guo, Yuan, Shen, Qu, & Xue, 2012), radioactive waste repositories (Neretnieks, 1993), and underground tunnels (Barton, Bandis, & Bakhtar, 1985; Fernandez & Moon, 2010). For the oil and gas industry, Naturally Fractured Reservoirs (NFRs) are of significant importance since approximately 60% of the remaining conventional oil and 40% of gas reserves in the world are hosted in fractured carbonates (Beydoun, 1998).

In many NFRs, the fractures act as the main pathways for fluid flow, especially in low permeability rocks. Rock fractures, have rough walls and variable apertures with asperities on the fracture walls which may be sustaining the fracture openings. The permeability of a rock fracture depends on the aperture distribution, surface roughness and contact area, all of which are functions of the stresses that act on the fracture walls. Thus, permeability can increase or decrease with stress depending on the confining stress and fluid pressure (Min, Rutqvist, Tsang, & Jing, 2004).

The change in the aperture due to stress can cause many orders of magnitude change in the hydraulic conductivity at moderate levels of compression (Barton et al., 1985). Zhang and Sanderson (1996) studied the effect of stress on the 2D permeability of fractured rocks considering the influences of burial depth, i.e. different levels of overburden pressure (S_v), differential stress, and loading direction. They defined normal and shear stiffnesses on the interface of 2D blocks which enabled them to calculate the amount of normal and tangential displacement between two adjacent blocks based on the block geometry and block centroid translation and rotation. They noticed that the permeability of the studied systems reduces with depth (i.e. increase of S_v) and that the differential horizontal stresses significantly influence the direction and magnitude of permeability. They observed that for a constant value of minimum horizontal stress, S_h, an increase of the maximum horizontal stress, S_H, reduces the network permeability. However, the method that Zhang and Sanderson (1996) used only takes into account the displacement and rotation at the aerial centroid of each block that results from the shear and normal *in situ* stresses. This is independent of the displacements/rotations of the other blocks which means that for fragmented rocks, the position of the blocks is not updated due the interactions between the blocks. This ignores the progressive deformation/rotation of a group of blocks which could be significant. Lang et al. (2012) also investigated permeability changes accompanying small displacements. They observed that stress dependent fracture opening/closing of medium to small scale fractures is critical for the permeability of the fracture-rock matrix ensemble.

Another group of methods for modelling fluid flow through fractures are the dual continua models. Zhang et al. (2002) conducted a 2D numerical study to model a large number of polygonal small blocks connected at their boundaries. The boundaries were the path for fluid transport. The blocks were defined to be deformable and tensile and shear limits were defined at boundaries which were broken when associated stresses reached a certain limit. Pre-existing fractures were also embedded into the model. They investigated the influence of differential stress and fluid pressure on the creation and propagation of fractures and fracture networks finding that high fluid pressure can cause the initiation and growth of fractures leading to the formation of a connected fracture network under. High differential stresses also promoted the initiation and growth of fractures with a significant influence on flow patterns.

Stress-dependent permeability of fractured rocks was investigated by Latham et al. (2013) considering the influence of fracture propagation and bending fractures in two-dimensional (2D) space. Combining the geomechanical behaviour of the fracture network with its fluid flow properties they showed that some particular stress states can reactivate the pre-existing fractures and can change the system's permeability. Lei et al. (2017) also studied the influence of triaxial stresses on the permeability of a three-dimensional (3D) fractured rock layer which was created by extruding a 2D outcrop pattern. They considered the influence of stress on the permeability of the fractured rock layer running a decoupled geomecahincal and flow analysis. The discrete element method that they used for the geomechanical modelling is capable of modelling the deformation of matrix blocks, variation of stress fields and propagation of fractures.

In this study, the change of fracture aperture in fragmented rocks has been investigated using Finite Element Analysis (FEA) while overcoming some of the common deficiencies of the older models including unrealistic boundary conditions due to 2D modelling, resolving far-field stresses on fractures ignoring the stress variations in rock layers, and ignoring block displacements and rotations.

To create more realistic boundary conditions, a sample fragmented rock layer is modelled in three dimensions by extruding a 2D fracture network which is placed between two softer shale layers. The horizontal stresses in different orientations and overburden pressure are applied. In addition to considering the influence of tri-axial stress states, this enables considering the influence of the compressibility of the neighbouring layers and the contrast between the elastic properties of the rock layers on the fracture apertures of the fragmented rock layer.

The variation of stress within the rock layer is simulated in a newly constructed mechanical model of the fragmented rock and analysing it under realistic boundary stresses. This is ignored in models which simply project far field stresses on the fractures (e.g. *Azizmohammadi and Matthäi* (2017)). Frictional interfaces are defined between the rock blocks, also permitting opening and closing of the fractures in addition to frictional sliding. Creating such a mechanical modelling, the deformations, displacements, and rotations of rock blocks can be estimated. This also enables a higher accuracy estimation of fracture dilation using Barton et al. (1985) method, as the shear displacements and normal stresses are calculated for individual fractures as part of the mechanical analysis.

After conducting the complex mechanical modellings, the updated maps of fracture apertures are obtained. Single-phase flow analysis is conducted for each case in two perpendicular directions to obtain the updated ensemble permeability. The tensorial permeability for each case is obtained and comparisons between the permeability tensors of different cases are conducted.

2 Methodology

The influence of *in situ* stress on the permeability of a fragmented rock layer was modelled in two steps. In the first step, three-dimensional linear-elastic mechanical finite element analyses were conducted using ABAQUS^{TM} applying the *in situ* stresses to the rock layers. Conducting this modelling in three dimensions, it was possible to simulate the simultaneous influence of the overburden and horizontal stresses. Frictional contacts were defined between the rock layers and the individual rock blocks of the fragmented layer. This enabled the simulation of the rotation and the relative displacement of individual blocks.

In the second step, the permeability of the fragmented rock layer was calculated by conducting a single phase flow simulation on the updated geometry, calculated in the previous step, to obtain the permeability tensor of the fragmented rock layer. Since, the fragmented rock layer is assumed to be the permeable layer of the model with flow occurring in its plane, with minimal flow in normal direction to it, this step was performed in 2D. This analysis was conducted using Complex Systems Modelling Platform (CSMP++) (S. K. Matthäi et al., 2007).

2.1 Finite Element Analysis (FEA)

A displacement based linear elastic finite element method was used to solve the undrained linear poroelasticity equations over the domain of interest. Static equilibrium is described by Cauchy's equation in vectorial form (Malvern 1969):

$$\nabla \underline{\sigma} + \boldsymbol{F} = 0 \tag{1}$$

where $\underline{\sigma}$ is the 3×3 second order tensor of total stress and $\boldsymbol{F}$ is the vector of body forces that act on the rock volume. In general, $\sigma_{ij} = \sigma_{ji}$; hence the stress tensor has only six unknown components while three equations are given. The three other equations required, can be derived using the tensorial form of Hooke's law, formulated by G. Lamé which is applicable for undrained porous materials (Ji, Sun, Wang, & Marcotte, 2010):

$$\sigma_{ij} = \lambda \varepsilon_{vol} \delta_{ij} + 2G\varepsilon_{ij} \tag{2}$$

In the above equation, λ is the Lamé parameter, δ_{ij} is the Kronecker delta (equals to 1 if $i = j$ and equals to 0 if $i \neq j$), G is the shear modulus and ε_{vol} is the volumetric strain which is the summation of the diagonal components of the strain tensor. Values of Lamé parameter and shear modulus for common rocks are available in different sources such as (Ji et al., 2010). These parameters can also be written in terms of other common mechanical properties such as elastic modulus (E) and Poisson's ratio (υ) as shown below

$$\lambda = \frac{E\upsilon}{(1+\upsilon)(1-2\upsilon)} \tag{3}$$

$$G = \frac{E}{2(1+\upsilon)} \tag{4}$$

Components of strain tensor are derived from displacements of the solid phase by the following definitions, where (u,v,w) is the displacement vector. Note that here a steady-state case of undrained material is assumed for which there is no fluid movement.

$$\begin{aligned}
\varepsilon_x &= \frac{\partial u}{\partial x}\,; \qquad \varepsilon_{xy} = \frac{\gamma_{xy}}{2} = \frac{1}{2}\left(\frac{\partial u}{\partial y} + \frac{\partial v}{\partial x}\right) \\
\varepsilon_y &= \frac{\partial v}{\partial y}\,; \qquad \varepsilon_{yz} = \frac{\gamma_{yz}}{2} = \frac{1}{2}\left(\frac{\partial v}{\partial z} + \frac{\partial w}{\partial y}\right) \\
\varepsilon_z &= \frac{\partial w}{\partial z}\,; \qquad \varepsilon_{zx} = \frac{\gamma_{zx}}{2} = \frac{1}{2}\left(\frac{\partial w}{\partial x} + \frac{\partial u}{\partial z}\right)
\end{aligned} \tag{5}$$

Substituting equation (5) into (2) reduces the number of unknowns to three, which, if inserted into equation (1), can be solved.

2.2 Frictional Interfaces

Frictional interfaces are defined where two different objects are likely to contact. This includes the interface between the different rock layers and at the fracture walls. The behaviour of frictional interfaces comprises of a no-penetration rule using a penalty algorithm to avoid interpenetration in the normal direction and a frictional behaviour in the tangential direction. A basic Coulomb friction model is used with the tangential stress required for sliding given by the following equation (Coulomb, 1773):

$$\tau = f(\sigma_n - p_f) \tag{6}$$

where τ is the tangential stress, f is the friction coefficient, σ_n is the stress normal to the considered surface, and p_f is the fluid pressure in the fracture. Byerlee (1978) showed that for a very wide range of rock types at high effective normal stresses (≥ ~10MPa), the friction coefficient is independent of surface roughness, normal stress, rate of slip, etc., and it is generally between 0.6 and 1.0. Here, a value of 0.6 is used conservatively. The effective stress is used here as the fracture fluid pressure counteracts the fracture normal stress. An earlier implementation of frictional interfaces between rock layers can be found in Agheshlui and Matthai (2017).

2.3 Dilation Effect

The FE modelling conducted in this research provides estimates of the normal and shear displacements of individual fractures. However, the shear dilation effect is not resolved by standard FE models because of a few order of magnitude difference in the scale of asperities and fragmented rock blocks which makes it impractical to include asperities directly into the block geometry. To overcome this problem, constitutive models developed based on experimental data by Barton et al. (1985) is used in this research. This model estimates the dilation values from the shear displacement and normal stress acting on fracture walls. Other parameters used in this model are Joint Roughness Coefficient (JRC_0), Joint wall Compressive Strength (JCS_0) and unconfined rock compressive strength (UCS). The model developed using $JRC_0 = 10$, $JCS_0 = 75$MPa, and UCS = 150MPa by *Barton et al.* (1985) is reproduced and displayed here in **Figure 1**. This model is used to calculate the fracture dilation as a function of shear displacement and fracture normal (effective) stress as obtained from the mechanical FE model.

2.4 Ensemble Permeability

A Discrete Fracture and Matrix (DFM) model was used for obtaining the ensemble permeability. For this, the fractures were represented by lower dimensional elements compared to the matrix (Stephan K. Matthäi & Nick, 2009; Paluszny, Matthai, & Hohmeyer, 2007). The permeability of individual fractures was computed from their aperture, a, using the parallel plate law (Kranzz, Frankel, Engelder, & Scholz, 1979):

$$k_f = \frac{a^2}{12} \tag{7}$$

To obtain the full permeability tensor of the ensemble, two steady-state flow problems were solved in two perpendicular directions. The ensemble absolute permeability tensor, $\mathbf{k}^E$ (8), was computed by solving Darcy's law (9), modified for the volume-averaged fluid velocity ($\mathbf{u}$), pressure gradient (∇p), and viscosity (μ), where $\langle\ \rangle$ is the volume averaging operator (Azizmohammadi & Matthäi, 2017; Durlofsky, 1991).

$$\mathbf{k}^E = \begin{bmatrix} k_{xx}^E & k_{xy}^E \\ & \\ k_{yx}^E & k_{yy}^E \end{bmatrix} \tag{8}$$

$$\langle \mathbf{u} \rangle = -\frac{\mathbf{k}^E}{\langle \mu \rangle} \cdot \langle \nabla p \rangle \quad (9)$$

Equation (9) in matrix form can be written as:

$$\begin{bmatrix} \langle \nabla p_x \rangle^1 & \langle \nabla p_y \rangle^1 & 0 & 0 \\ 0 & 0 & \langle \nabla p_x \rangle^1 & \langle \nabla p_y \rangle^1 \\ \langle \nabla p_x \rangle^2 & \langle \nabla p_y \rangle^2 & 0 & 0 \\ 0 & 0 & \langle \nabla p_x \rangle^2 & \langle \nabla p_y \rangle^2 \end{bmatrix} \begin{Bmatrix} k_{xx}^E \\ k_{xy}^E \\ k_{yx}^E \\ k_{yy}^E \end{Bmatrix} = -\langle \mu \rangle \begin{Bmatrix} \langle u_x \rangle^1 \\ \langle u_y \rangle^1 \\ \langle u_x \rangle^2 \\ \langle u_y \rangle^2 \end{Bmatrix}, \quad (10)$$

where superscripts 1 and 2 denote the two flow directions.

3 Model Description

3.1 Mechanical Modelling

A 4.5m×4.0m section of Kilve outcrop was selected for studying the stress influence on fracture apertures in the fragmented rock layer. The corresponding 3D model consists of a layer of fragmented brittle limestone rock extruded in the normal direction with a thickness of 0.2m sandwiched between two plastic shale layers with thicknesses of 1m. The fracture walls are assumed to be in contact before the *in situ* stress is applied. All fractures were considered to end at the intersection with other fractures and to be confined, i.e. they terminated at the layer boundaries in the vertical direction. Figure 2 (a) shows the plane view of the fragmented rock layer and Figure 2 (b) depicts the entire model including the fragmented layer and the plastic top and bottom layers.

Frictional contact surfaces were defined at the interfaces of the blocks and the rock layers. Defining this, the movement of blocks relative to each other under the applied stresses was simulated while updating the geometry of the entire fragmented rock layer due to the movement of individual blocks. Hence, modelling the change in the aperture was made possible with a much higher level of accuracy.

The model was created in 3D so that overburden and horizontal stresses could be applied simultaneously. This was because in addition to the shear and normal components of the horizontal stresses which affect the fracture apertures, the overburden stress also influences them by the differential displacements that occur at the interface of layers due to their different mechanical properties. The mechanical and hydraulic properties of the rock layers of the model are given in Table 1. The model was assumed to be located at a depth of 2km with an average overburden dry density of 2200 kg/m^3 which creates an overburden pressure of S_v= 43.16 MPa applied to its top surface. Horizontal stresses of $S_H = 0.85\times S_v =$ 36.7 MPa and $S_h = 0.7\times S_v =$ 30.2 MPa were assigned to the side walls of the model to replicate an extensional tectonic regime (Figure 2(b)). The fluid pressure in the fractures was taken as hydrostatic with a brine density of 1100 kg/m^3. Furthermore, a hydrostatic pore pressure was assumed to exist in the entire model.

3.1.1 Creating the model

To build the model the following steps were taken: (1) the fracture geometry was created by importing individual blocks from CAD applications and adding the confining shale layers above and below in ABAQUS; (2) a poro-elastic material model was assigned to the limestone and shale layers; (3) limestone and shale layers were adaptively meshed using quadratic hexahedral and wedge elements to a resolution that further reduction in element sizes made only minimal changes in results (see **Figure 3**); (4) frictional interfaces were defined between all the individual blocks and the neighbouring layers, employing a penalty algorithm (Kikuchi, 1982) to avoid block interpenetration; a basic Coulomb friction model (Coulomb, 1773) was applied to contacting surfaces; (5) displacement and stress boundary conditions were applied to the model including constrained displacements in all directions at the base, constrained displacements in X and Y directions at the top surface, overburden stress, S_V, applied to the top surface, boundary stresses of S_H and S_h applied to the model side walls; (6) hydrostatic pore pressure was defined in the model; (7) fracture fluid pressure was applied as surface pressure to the side walls of the individual rock blocks; (8) simulations were run using unsymmetric solvers and a displacement convergence criterion was chosen with a maximum residual factor of 0.005; outputs were post-processed for the use in the flow simulations.

The mesh, shown in **Figure 3**, was adaptively refined to capture the details around corners and complex geometries where high variations were expected. The maximum element length (in the fracture network plane) was limited to 80mm and element thickness (perpendicular to the fracture network plane) was limited to 40mm, i.e. five elements to capture stress variations within the thickness of the limestone layer. The mesh included 94125 hexahedral and 605 wedge elements. A 20% further reduction in the element length resulted only in 0.2% change in the maximum displacement of the limestone layer observed at its top right corner.

3.1.2 Orientation of Horizontal Stresses

As shown by Zhang and Sanderson (1996), the change in the orientation of the horizontal stresses acting on the fracture patterns could change the permeability of fractured rocks significantly. To study this effect while considering more realistic 3D boundary conditions, eight different orientations for horizontal stresses were considered with intervals of 22.5 degrees as shown in Figure 4.

3.2 Flow Modelling

For flow modelling, the Complex Systems Modelling Platform (CSMP++, Matthai et al. (2007)) was used as a basis for the computation of pressure and velocity fields. A Discrete fracture and matrix (DFM) model of the geometry shown in Figure 2(a) was built. Although the mechanical modelling was done in 3D, to reduce the computational time and assuming a constant flow over the fracture depth, the flow modelling was conducted in 2D. It is worth noting that all the fractures were assumed to be confined, i.e. fully developed over the thickness of the limestone layer. A linear representation, lower dimensional elements compared to the matrix, was used for fractures as it is used in DFM models (Stephan K. Matthäi & Nick, 2009; Paluszny et al., 2007). The rock properties and saturation were discretized as piecewise constants on the elements while fluid pressure was discretized as piecewise linear on the nodes and computed with the FEM (e.g. Zienkiewicz, Taylor, and Taylor (1977)). Flow velocities were obtained by post-processing the pressure gradients using Darcy's law. The Complex Systems Modelling Platform (CSMP++) calculates pressure and velocity fields using the Bubnov-Galerkin finite-element method, see Matthai and Belayneh (2004). This approach has been verified with analytical solutions for periodic anisotropic porous media (Lang et al., 2014) and has also been used by Milliotte et al (2018) in their fracture and matrix modelling workflow.

For each stress regime, fracture apertures over the sides of all the blocks were calculated from the geomechanical modelling and then were input into the flow simulations. Having the aperture, the permeability of the fractures was computed using the parallel plate law, equation (7). Fractures with apertures lower than 0.025 millimetre were assumed to be closed and their properties were set to be the same as the matrix ($k=10^{-13}$, $\phi=0.2$).

As mentioned earlier, to obtain the permeability tensor, a steady-state flow problem was solved in two perpendicular directions, X and Y, defined in Fig 1(a). For each direction, constant pressure Dirichlet boundary conditions were applied to the model edges perpendicular to that direction while no-flow (natural) boundary conditions were assigned to the other two edges. First, the pressure field was solved using the finite element method. Then the velocity field was calculated by post-processing the pressure gradients using Darcy’s law. Here, a pressure gradient of 220 Pa/m was set across the model for each flow problem (left to right for the flow in the X direction and bottom to top for the flow in the Y direction). The fluid used here was water with a viscosity of 0.001 Pa.s.

4 Results

4.1 Stress orientation effect (α)

The deformation shape of the fragmented rock layer for α =22.5º case is shown in Figure 5. This figure demonstrates how horizontal stresses with shear and normal components can cause the individual blocks to move and rotate which in turn influences the entire fragmented rock layer. Depending on the magnitude of the stresses on the surfaces of the individual blocks, and based on the implemented Coulomb friction model, the blocks may start sliding relative to each other. Also, the distribution of Von-Mises stresses in the fragmented rock layer due to applied *in situ* stresses for all the considered horizontal stress orientations are shown in Figure 6. The fracture normal openings were calculated from mechanical simulations. As mentioned earlier, openings due to the fracture dilations were calculated using the model developed by Barton et al. (1985). The total amount of calculated fracture openings are shown in Figure 7. To demonstrate the difference between the distribution of fracture apertures, histograms of fracture apertures for cases of α=0º and α=45º are shown in Figure 8.

The obtained fracture apertures were applied to the DFM models. Running the flow simulations, the ensemble permeabilities for each stress orientation was obtained. Table 2 lists the components of the permeability tensor for each horizontal stress orientation. As it can be seen in Figure 11, for the cases of α=0º and α=90º for which horizontal stresses are normal to the model edges, most of the fractures are closed. This has resulted in very small values of permeability as shown in Table 2. The values of permeability in both X and Y directions are very close to the matrix permeability ($k=1\times10^{-13}$). However, for the cases where the horizontal stresses are not perpendicular to the model edges (the direction of major fractures), a significant number of fractures have opened which has resulted in larger permeabilities. For α=22.5°, k_{xx} and k_{yy} were increased by 35% and 16%, respectively, compared to α=0º. The off-diagonal terms were increased by one order of magnitude. For α=45°, k_{xx} and k_{yy} were 118% and 69% larger than the corresponding values for α=0º. For α=67.5º, the components of permeability tensor were still significantly larger than the values for α=0º, however they were reduced compared to α=45°.

Checking the trend for permeability components in Table 2, it can be observed that the maximum permeabilities were obtained for α=45º and α=135º, for which the shear component of horizontal stresses was the largest. The largest permeability in X and Y directions occurred in α=45º and α=135º, respectively. These are the stress orientations which produce the largest normal openings in major fractures.

The principal values of the permeability tensors (i.e. the eigenvalues: λ_{max} and λ_{min}) vary with the stress orientation, α, as well (Table 2). The highest values for λ_{max} and λ_{min} occur at α=45°, and α=135° and the lowest values occur at α = 0°, and α = 90°. This considerable change in the principal values of the permeability tensor is due to the significant effect of the horizontal stress orientation on the fracture network as clearly illustrated in Fig. 5.

As it can be observed in Table 2, the permeability tensor is not symmetrical. However, since the difference between the off-diagonal terms is insignificant, it may be assumed that the tensor is symmetrical. The tensors can be plotted as ellipses using the eigenvectors of the permeability tensors as shown in Figure 13. The influence of shear stresses on the model permeability can clearly be seen as the very large and elliptical shape of α =45° and α =135° cases. For the cases of α =22.5°, α =67.5°, α =112.5° and α=157.5° which there is still significant shear stress components, the graphical representation of the permeability tensor is still elliptical. However, for the cases of α =0° and α =90°, the shapes are almost circular. Here, the system is almost isotropic for permeability with very close values of λ_{max} and λ_{min}.

The Anisotropy Ratio (AR) in permeability tensors can be shown by an anisotropy ratio (AR = $\frac{\lambda_{max}}{\lambda_{min}}$,) (M. Sedaghat, 2017) . Figure 10 shows AR versus α for the model. As it was also shown in **Figure 9**, the model is approximately isotropic in terms of permeability when the horizontal stresses are perpendicular to the model edges (i.e. α = 0°, and α = 90°).

The maximum anisotropy occurs at 45°, and 135° stress orientations with $\mathrm{AR}_{\alpha=45} > \mathrm{AR}_{\alpha=135}$. However, the global direction of permeability tensor does not change significantly even for these cases.

4.2 Influence of the Mechanical Properties of the Top and Bottom Layers

To demonstrate the influence of the mechanical properties of the neighbouring top and bottom rock layers on the fracture opening of the brittle fragmented layer, three different models were analysed. The case with α=22.5º was used for this study. Table 3 shows the mechanical properties used for these three models. In the first case, Shale-1 (the same as α=22.5º), the reference mechanical properties, given in Table 1, were used. For the second case, Shale-2, the elastic modulus and for the third case, Shale-3, the Poisson's ratio of the top and bottom shale layers were changed.

The Von-Mises stress distribution for these three cases are shown in Figure 11. The fracture apertures for these three cases are illustrated and compared in Figure 12. **Table 4** presents the permeability tensors and eigenvalues for these three cases. Figure 13 shows the graphical representation of the permeability tensors which is obtained using the eigenvectors of permeability tensors.

4.3 Influence of rock deformation on ensemble permeability

Here, using deformable rock blocks and analysing the entire rock layer under the *in situ* stresses, the influence of block deformations on the fracture apertures were considered. However, in some other research works, the *in situ* stresses are directly projected on the fracture surfaces without considering the rock deformation (Azizmohammadi & Matthäi, 2017). To quantify the effect of ignoring the block deformations, a comparative study is conducted here for the α=22.5º case, named *α=22.5º-Solid Blocks*. Using a significantly stiffer material (E=10×$E_{Fragmented\ Rock}$), the rock deformations were reduced to a minimal level similar to when the deformations are ignored. The aperture map for this case is shown in Figure 14. The components of the permeability tensor for the cases of α=22.5º and *α=22.5º-Solid Blocks* are shown and compared in Table 5. As can be seen, significant errors in permeability may occur if the block deformations are ignored. Interestingly, when the block deformations are ignored, the diagonal components of the permeability tensor, i.e. k_{xx} and k_{yy}, increase. The reason for this could be that since the blocks cannot deform, they undergo larger solid movements and rotations which results in further openings in fractures.

5 Discussion

Historically the flow simulations in fractured and fragmented rocks have been conducted by making simplifications on mechanical modelling or by ignoring the mechanics-flow interaction altogether. Some of the common simplifications that their effect is investigated in this paper are:

(a) two-dimensional modelling while ignoring the actual triaxial stress states, e.g. Sanderson (1996), Zhang et al. (2002), *Latham et al.* (2013), and *Min et al.* (2004).

(b) considering the stress influence on fracture apertures by projecting *in situ* stresses on fractures and using stiffness relationships in shear, normal and dilation behaviours (e.g. Barton et al. (1985)), without conducting mechanical analysis of the solid phase, e.g. Azizmohammadi and Matthäi (2017); and
(c) not considering the influence of the neighbouring layers with different mechanical properties which is inevitable in 2D studies.

These simplifications are normally done to reduce the computational cost while still getting an approximation of the change of apertures due to the *in situ* stresses. As a result, the actual change of aperture is not estimated accurately. To demonstrate the effect of such simplifications, a qualitative comparison is conducted here against the results available in the literature from Azizmohammadi and Matthäi (2017). The study undertaken by Azizmohammadi and Matthäi (2017) was done on the Kilve outcrop, 8m×18m, assuming S_H = 15 MPa, S_h = 10 MPa and α=45º. The same study was repeated here, however on a 4.5m×4m portion of the same outcrop, using the same horizontal stresses while assuming $S_H = 0.9\times S_v$, $S_h = 0.6\times S_v$ which results in S_v = 16.67 MPa. Although there are differences between these models, the comparison shown in Figure 15 demonstrates the significance of the differences that may exist between the results. As it can be seen, the fractures in the Azizmohammadi and Matthäi (2017) model are much larger and almost all of them have opened up. Whereas in the full mechanical modelling conducted here, the fracture apertures are much smaller and in some cases, they have not even been opened.

It should also be noted that conducting analysis in 2D inevitably results in ignoring the influence of overburden stresses on fracture apertures. Whereas, fracture apertures, in addition to being dependant on horizontal stresses, are also strongly dependant on overburden stresses due to the Poisson's effect. The overburden stress results in lateral expansion of the rock layers. In the case of this study, this causes a relatively larger lateral expansion in the plastic shale layers which displaces the rock blocks in the fragmented rock layer and increases the fracture apertures. This effect cannot be considered in 2D modellings. Hence, as also mentioned by Lei et al. (2017), results from 2D models may only provide indicative approximations. It is worth noting that in this study all the fractures were initially assumed to be closed. Depending on the *in situ* stresses applied and the mechanical properties of the rock layers, some of the fractures were opened and contributed to the ensemble permeability.

The strong importance of considering the three-dimensional stress state on the fracture apertures and the ensemble permeability was also shown by demonstrating the sensitivity of the fracture apertures and ensemble permeability to the elastic modulus and the Poisson's ratio of the neighbouring layers (Table 4, Figure 12 and Figure 13). A larger difference in elastic moduli as well as the Poisson's ratios increased the apertures and the ensemble permeability and vice versa. Bai et al. (2000) also reported the influence of the difference in elastic moduli. However, they suggested that the fracture apertures for their study was not sensitive to the difference in Poisson's ratios which may not be true for all cases since this is the coefficient that defines the lateral expansion of the neighbouring layers and has a direct influence on fracture apertures.

The influence of the block deformations on the ensemble permeability was also investigated in this research. It was found that if the blocks are solid, i.e. the strain energy cannot be absorbed by block deformations, they will undergo relatively larger displacements and rotations which can result in considerably larger fracture apertures and ensemble permeabilities. This suggests that the fracture aperture calculations ignoring the deformability of blocks in fragmented rocks may result in considerable errors.

Results from this research also show that the fracture apertures and the permeability tensor of fragmented rocks are significantly influenced by the orientation of the horizontal *in situ* stresses. In favourable directions, i.e. the directions with large shear stress components, a considerable increase in permeability was observed. In the X direction (direction with long continuous fractures) the maximum permeability ratio to the minimum one was found to be 2.19. The same value for the Y, XY and YX directions were 1.72, 19.58 and 17.87 respectively. Similar patterns were reported by other researchers such as Zhang and Sanderson (1996) and Zhang et al. (2002) which showed that dilatational shearing is an important mechanism in holding fractures open under a fluid pressure lower than the confining pressure.

In this research permeability was computed using a tensorial approach (Durlofsky, 1991) after finding the fracture apertures from a full mechanical model. Permeability could have also been computed using a conventional method (e.g. (M. H. Sedaghat, Azizmohammadi, & Matthäi, 2017)). However in that case the permeabilities in the horizontal and vertical directions, k_h and k_v respectively, might have been different form k_{xx} and k_{yy}, especially for α=45° and α=135° where the off-diagonal terms are relatively large (M. H. Sedaghat et al., 2017). In addition, it should be noted that the symmetry condition ($k_{xy} = k_{yx}$) proposed by (Onsager, 1931) was not applied for the permeability analysis in here since the permeability tensor is not symmetrical in general. It should be noted that applying the symmetry condition can result in changes in the components of the permeability tensor, especially for the cases with relatively large off-diagonal components.

Permeability tensors can be presented as ellipses as already done in the literature (see (Azizmohammadi & Matthäi, 2017; P. S. Lang et al., 2014)). Since the computed permeability tensors in here are not symmetrical, their eigenvectors are not necessarily orthogonal. Depending on the magnitude of the off-diagonal terms of the permeability tensor, this may cause different effects on the graphical representation of the permeability tensor. To the best of the knowledge of the authors, a general method for the graphical representation of the non-symmetrical permeability tensors was not developed at the time of this research. Nonetheless, since the off-diagonal terms were almost equal and their values were insignificant compared to the diagonal components, the elliptical representation should be reasonably accurate.

As limitations of this work, we should mention that here all the sealed fractures have been assigned the same properties of the matrix. However, crushing and grinding of the matrix blocks can create sealed fractures with very low permeabilities. This can significantly reduce the ensemble permeability in both directions, making the absolute permeability ellipses to shrink. Also, compression of matrix blocks under the *in situ* stresses can further reduce the rock properties within the blocks, consequently shrinking the ellipses furthermore. Having established these stress-strain-rock properties relations, can make the modellings conducted here more realistic.

It should also be mentioned that in this work, only a portion of the outcrop was modelled and the entire model was considered as a coarse grid. No attempt was made to determine the representative elementarily volume (REV) of the entire model.

Figure **6** clearly shows that the stress magnitudes at model sides were higher than the values in the middle part of the model. Hence, if permeability tensors were to be calculated for different parts of the model, different values might have been obtained. So, conducting an REV analysis (see Azizmohammadi & Matthai (2017)) may help with determining the actual size of the coarse grid. Furthermore, the 3D mechanical model used here was created by extruding a 2D fracture model whereas in reality the fracture aperture may also change through the thickness of the fractures.

6 Conclusion

In this research, the influence of the *in situ* stresses on fracture apertures and ensemble permeability of the fragmented rocks was studied. The tensorial permeability of a fragmented rock layer was obtained for all the considered cases. Some of the influential simplifying assumptions used in earlier research works on this topic were replaced with more realistic ones. A 3D mechanical model of the fragmented rock layer was created including the neighbouring layers. This enabled the modellings to consider the realistic 3D boundary conditions as well as the influence of the differential deformations of rock layers on the fracture apertures of the fragmented rock layer. Also, frictional interfaces were defined between rock layers and the rock blocks which made it possible to model the displacements and rotations of individual blocks and their influence on the geometry of the entire rock layer and its ensemble permeability. The deformation of the rock blocks was also modelled using the mechanical model.

It was demonstrated that the overburden stress creates lateral expansion of the neighbouring layers as well as the considered fragmented layer which increases the fracture apertures. Hence, it was concluded that considering the triaxle nature of the *in situ* stresses is critical in obtaining realist estimations of the ensemble permeability.

The mechanical properties of neighbouring layers were also found to be important on the aperture size of the fragmented rock layer. A lower elastic modulus and a higher Poisson's ratio for the neighbouring layers resulted in larger fracture apertures for the fragmented rock layer. For an almost solid fragmented rock layer (negligible block deformation), since the rock blocks could not deform, they underwent larger displacements and rotations which resulted in a higher permeability for the fragmented rock layer.

The influence of the orientation of the horizontal *in situ* stresses was also investigated on the ensemble permeability of a fragmented rock layer. It was shown that the large shear forces applied due to the favourable orientation of horizontal *in situ* stresses can result in the opening of the initially closed fractures and can increase the ensemble permeability significantly.

It was concluded that estimating stress influence on fracture apertures using 2D models, ignoring the block deformations, displacements and rotations, as well as the local stress variations/concentrations may result in considerable errors.

Acknowledgement

No new data were used in producing this manuscript.

References

Agheshlui, H., & Matthai, S. (2017). Uncertainties in the estimation of in situ stresses: effects of heterogeneity and thermal perturbation. *Geomechanics and Geophysics for Geo-Energy and Geo-Resources*. doi:10.1007/s40948-017-0069-z

Azizmohammadi, S., & Matthäi, S. K. (2017). Is the permeability of naturally fractured rocks scale dependent? *Water Resources Research*, n/a-n/a. doi:10.1002/2016WR019764

Bai, T., Pollard, D. D., & Gross, M. R. (2000). Mechanical prediction of fracture aperture in layered rocks. *Journal of Geophysical Research: Solid Earth, 105*(B1), 707-721. doi:10.1029/1999JB900303

Barton, N., Bandis, S., & Bakhtar, K. (1985). Strength, deformation and conductivity coupling of rock joints. *International Journal of Rock Mechanics and Mining Sciences & Geomechanics Abstracts, 22*(3), 121-140. doi:http://dx.doi.org/10.1016/0148-9062(85)93227-9

Beydoun, Z. R. (1998). Arabian plate oil and gas: why sorich and soprolific? *Episode, 21*(6), 74-81.

Byerlee, J. D. (1978). Friction of rock. *Pure & Applied Geophysics, 116*(615-626).

Coulomb, C. A. (1773). Sur une application des regles de maximums et minimums a quelques problemes de statistique relatifs a larchitesture, Acad. Roy. *Sci. Mem. Mech. Min Sci., 7*(343-382).

Durlofsky, L. J. (1991). Numerical calculation of equivalent grid block permeability tensors for heterogeneous porous media. *Water Resources Research, 27*(5), 699-708. doi:10.1029/91WR00107

Fernandez, G., & Moon, J. (2010). Excavation-induced hydraulic conductivity reduction around a tunnel – Part 1: Guideline for estimate of ground water inflow rate. *Tunnelling and Underground Space Technology, 25*(5), 560-566. doi:http://dx.doi.org/10.1016/j.tust.2010.03.006

Guo, H., Yuan, L., Shen, B., Qu, Q., & Xue, J. (2012). Mining-induced strata stress changes, fractures and gas flow dynamics in multi-seam longwall mining. *International Journal of Rock Mechanics and Mining Sciences, 54*, 129-139. doi:http://dx.doi.org/10.1016/j.ijrmms.2012.05.023

Ji, S., Sun, S., Wang, Q., & Marcotte, D. (2010). Lamé parameters of common rocks in the Earth's crust and upper mantle. *Journal of Geophysical Research: Solid Earth, 115*(B6), n/a-n/a. doi:10.1029/2009JB007134

Kazemi, H., & Gilman, J. R. (1993). Multiphase flow in fractured petroleum reservoirs. In J. Bear, C. F. Tsang, & G. d. Marsily (Eds.), *Flow and contaminant transport in fractured rocks* (pp. 267-323): Academic Press, San Diego, CA (United States).

Kikuchi, N. (1982). A Smoothing Technique for Reduced Integration Penalty Methods in Contact Problems. *Int. J. Num. Meth. Engng., 18*, 343-350.

Kranzz, R., Frankel, A., Engelder, T., & Scholz, C. (1979). *The permeability of whole and jointed Barre granite.* Paper presented at the International Journal of Rock Mechanics and Mining Sciences & Geomechanics Abstracts.

Lang, P., Steinecker, S., Afkan, S. B., & Matthäi, S. K. (2012). *Stress dependent anisotropy of relative permeabilities in naturally fractured reservoirs* Paper presented at the ECMOR XIII - 13th European Conference on the Mathematics of Oil Recovery, Bairritz, France

Lang, P. S., Paluszny, A., & Zimmerman, R. W. (2014). Permeability tensor of three-dimensional fractured porous rock and a comparison to trace map predictions. *Journal of Geophysical Research: Solid Earth, 119*(8), 6288-6307. doi:10.1002/2014JB011027

Latham, J.-P., Xiang, J., Belayneh, M., Nick, H. M., Tsang, C.-F., & Blunt, M. J. (2013). Modelling stress-dependent permeability in fractured rock including effects of propagating and bending fractures. *International Journal of Rock Mechanics and Mining Sciences, 57*, 100-112. doi:http://dx.doi.org/10.1016/j.ijrmms.2012.08.002

Lei, Q., Wang, X., Xiang, J., & Latham, J. P. (2017). Polyaxial stress-dependent permeability of a three-dimensional fractured rock layer. *Hydrogeology Journal*, 1-12.

Matthäi, S., & Belayneh, M. (2004). Fluid flow partitioning between fractures and a permeable rock matrix. *Geophysical Research Letters, 31*(7).

Matthäi, S. K., Geiger, S., Roberts, S. G., Paluszny, A., Belayneh, M., Burri, A., . . . Heinrich, C. A. (2007). Numerical simulation of multi-phase fluid flow in structurally complex reservoirs. In S. J. Jolley, D. Barr, J. J. Walsh, & R. J. Knipe (Eds.), *Structurally Complex Reservoirs.* (Vol. 292, pp. 405–429): The Geological Society.

Matthäi, S. K., & Nick, H. M. (2009). Upscaling two-phase flow in naturally fractured reservoirs. *AAPG Bulletin, 93*(11), 1621-1632. doi:10.1306/08030909085

Mavko, G., Mukerji, T., & Dvorkin, J. (2003). *The Rock Physics Handbook: Tools for Seismic Analysis of Porous Media*: Cambridge University Press.

Milliotte, C., Jonoud, S., Wennberg, O., Matthäi, S., Jurkiw, A., & Mosser, L. (2018). Well-data-based discrete fracture and matrix modelling and flow-based upscaling of multilayer carbonate reservoir horizons. *Geological Society, London, Special Publications 459 (1),, 459*(1), 191-210.

Min, K.-B., Rutqvist, J., Tsang, C.-F., & Jing, L. (2004). Stress-dependent permeability of fractured rock masses: a numerical study. *International Journal of Rock Mechanics and Mining Sciences, 41*(7), 1191-1210. doi:https://doi.org/10.1016/j.ijrmms.2004.05.005

Neretnieks, I. (1993). Solute transport in fractured rock: Application to radionuclide waste repositories. In J. Bear, C.-F. Tsang, & G. d. Marsily (Eds.), *Flow and Contaminant Transport in Fractured Rock* (pp. 39-127). San Diego: Academic Press.

Onsager, L. (1931). Reciprocal relations in irreversible processes. *Physical review, 37*(4), 405.

Paluszny, A., Matthai, S. K., & Hohmeyer, M. (2007). Hybrid finite element–finite volume discretization of complex geologic structures and a new simulation workflow demonstrated on fractured rocks. *Geofluids, 7*(2), 186-208. doi:10.1111/j.1468-8123.2007.00180.x

Sedaghat, M. (2017). *The relative permeability of layered fractured rocks.* (PhD), The University of Melbourne,

Sedaghat, M. H., Azizmohammadi, S., & Matthäi, S. K. (2017). Numerical investigation of fracture-rock matrix ensemble saturation functions and their dependence on wettability. *Journal of Petroleum Science and Engineering, 159*(Supplement C), 869-888. doi:https://doi.org/10.1016/j.petrol.2017.10.013

Zhang, X., & Sanderson, D. J. (1996). Effects of stress on the two-dimensional permeability tensor of natural fracture networks. *Geophysical Journal International, 125*(3), 912-924. doi:10.1111/j.1365-246X.1996.tb06034.x

Zhang, X., Sanderson, D. J., & Barker, A. J. (2002). Numerical study of fluid flow of deforming fractured rocks using dual permeability model. *Geophysical Journal International, 151*(2), 452-468. doi:10.1046/j.1365-246X.2002.01765.x

Zienkiewicz, O. C., Taylor, R. L., & Taylor, R. L. (1977). *The finite element method* (Vol. 3): McGraw-hill London.

Tables

Table 1. Mechanical and hydraulic properties of rock layers used in the model (Mavko, Mukerji, & Dvorkin, 2003)

Rock type	Elastic Modulus, *E*, (GPa)	Poisson's ratio, υ, (-)	Porosity, $\boldsymbol{\phi}$, (-)	Permeability, *k*, (m^2)
Shale	10	0.4	0.05	1×10^{-14}
Limestone	20	0.25	0.15	1×10^{-13}

Table 2. Permeability tensors obtained at different horizontal stress orientation

α(°)	$\boldsymbol{k}\times10^{-13}$ (m^2)					
	k_{xx}	k_{xy}	k_{yx}	k_{yy}	λ_{max}	λ_{min}
0	1.0228	-0.0048	-0.0047	1.0166	1.025	1.014
22.5	1.381	-0.035	-0.031	1.188	1.386	1.182
45	2.233	0.094	0.017	1.713	2.339	1.707
67.5	1.566	0.027	0.024	1.321	1.568	1.318
90	1.0196	-0.0049	-0.0048	1.008	1.021	1.006
112.5	1.436	-0.041	-0.031	1.287	1.444	1.278
135	2.100	-0.061	0.084	1.735	2.101	1.734
157.5	1.417	0.023	-0.007	1.228	1.417	1.227

Table 3. Values used for sensitivity analysis on mechanical properties of rock layers

Mechanical properties	limestone	Shale-1	Shale-2	Shale-3
Elastic Modulus (GPa)	20	5	10	5
Poisson's ratio (-)	0.25	0.4	0.4	0.25

Table 4. Permeability tensors obtained at different scenarios

Test case	$\mathbf{k}\times10^{-13}$ (m^2)					
	k_{xx}	k_{xy}	k_{yx}	k_{yy}	λ_{max}	λ_{min}
Shale-1	1.381	-0. 035	-0. 031	1.188	1.386	1.182

Shale-2	1.145	-0. 0141	-0. 0221	1.051	1.148	1.047
Shale-3	1.183	-0. 0179	-0. 0242	1.059	1.186	1.056

Table 5. Permeability tensors obtained at different scenarios

Test	**k**×10^{-13} (m^2)					
	k_{xx}	k_{xy}	k_{yx}	k_{yy}	λ_{max}	λ_{min}
α = 22.5	1.381	-0. 035	-0. 031	1.188	1.386	1.182
α = 22.5 – Solid Blocks	2.146	0.021	0.027	1.521	2.146	1.520
Error (%)	55.4	Significant	Significant	28.0	54.8	28.6

Figure Captions

Figure 1. Dilation due to shear displacement for different levels of fracture normal stress (Barton et al. (1985))

Figure 2. Model of the fractured limestone at Kilve, lilstock, UK; (a) fracture map in plan view; (b) composite model of the segmented rock layer sandwiched between two soft layers in 3D

Figure 3. Discretization of the fragmented rock layer using a mesh of hexahedral and tetrahedral elements interfaced by prisms

Figure 4. Stress regimes applied to the fragmented rock network. Note that the overburden stress is applied perpendicular to the plane.

Figure 5. Deformation shape of the fragmented rock layer under horizontal stresses with $\alpha = 22.5^{\circ}$. Units are in meters and deformations are 50 times magnified. Notice the independent displacements and rotations of blocks and the kinked edges.

Figure 6. Von-Mises stress distribution (Pa) in the fragmented rock layers under different stress orientations. Note: deformation scale is 1.0. The stress colour spectra are the same for all figures.

Figure 7. Fracture apertures under different horizontal stress orientations. Note: thin black lines represent closed fractures.

Figure 8. Distribution of fracture apertures for two cases of $\alpha=0^{\circ}$ (left) and $\alpha=45^{\circ}$ (right)

Figure 9. Elliptical representation of permeability tensors ($\times 10^{-13}$ m^2) for Kilve model at different horizontal stress orientation (α).

Figure 10. Anisotropy ratio versus horizontal stress orientation

Figure 11. Von-Mises stress distribution (Pa) in the fragmented rock layers for different mechanical properties of top and bottom layers (α=22.5º). Note: deformation scale is 1.0. The stress colour spectra are the same for all figures.

Figure 12. Fracture apertures with different mechanical properties for the top and bottom layers. Note: thin black lines represent closed fractures.

Figure 13. Fracture apertures considering different mechanical properties for the neighboring layers

Figure 14. Comparison of Fracture apertures for α=22.5 case (Left) and solid blocks (Right). Note: thin black lines represent closed fractures.

Figure 15. Comparison of the fracture apertures obtained using a full mechanical model (Left), and using Barton et al. (1985) model without conducting a mechanical model (Right) (Azizmohammadi & Matthäi, 2017). Note: thin black lines represent closed fractures.

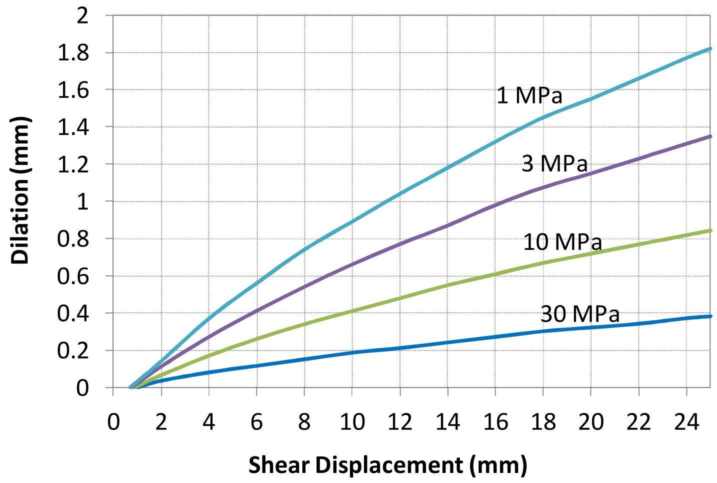

1 MPa
3 MPa
10 MPa
30 MPa
Dilation (mm)
Shear Displacement (mm)
0
0.2
0.4
0.6
0.8
1
1.2
1.4
1.6
1.8
2
0
2
4
6
8
10
12
14
16
18
20
22
24

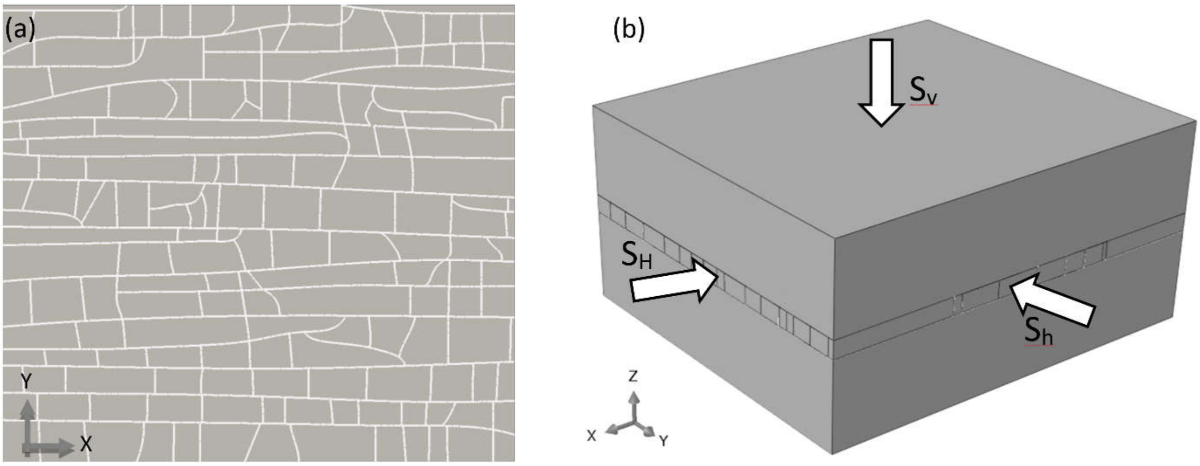

(a)
Y
X
(b)
Sv
SH
Sh
Z
X
Y

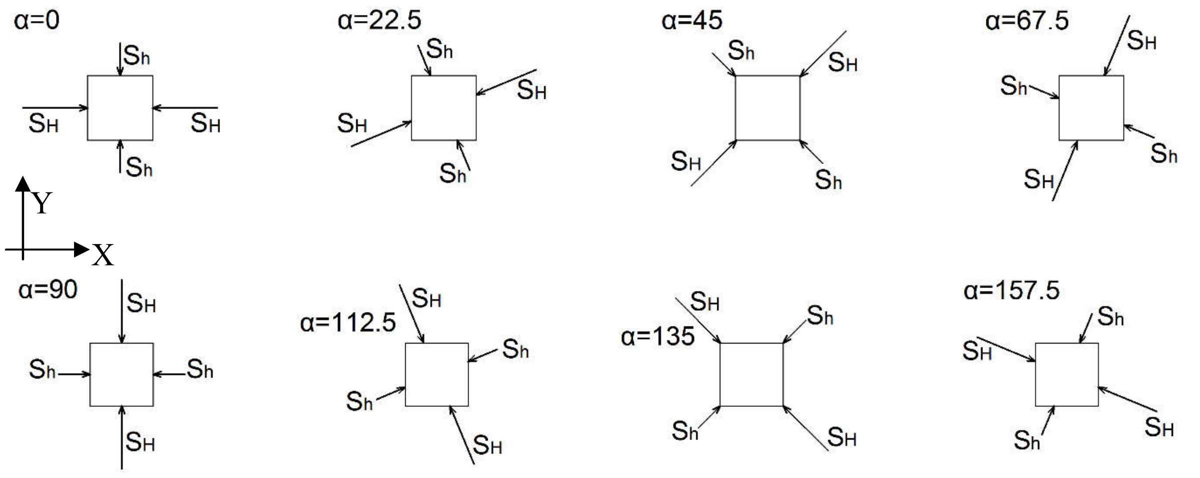

α=0
Sh
SH
SH
Sh
Y
X
α=22.5
Sh
SH
SH
Sh
α=45
Sh
SH
SH
Sh
α=67.5
SH
Sh
Sh
SH
α=90
SH
Sh
Sh
SH
α=112.5
SH
Sh
Sh
SH
α=135
SH
Sh
Sh
SH
α=157.5
Sh
SH
SH
Sh

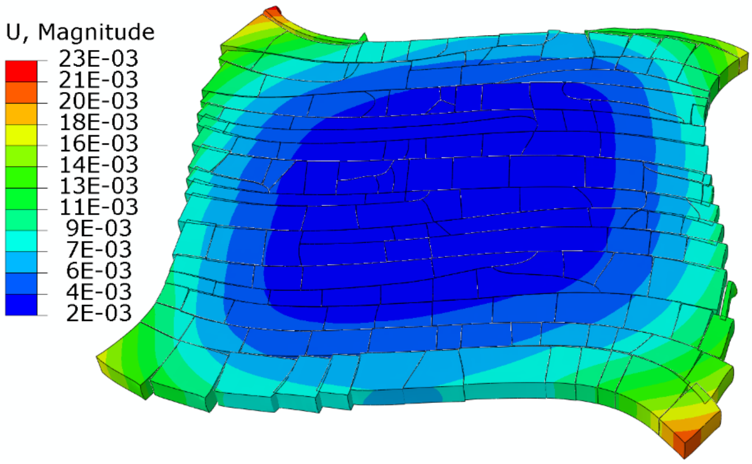
U, Magnitude
23E-03
21E-03
20E-03
18E-03
16E-03
14E-03
13E-03
11E-03
9E-03
7E-03
6E-03
4E-03
2E-03

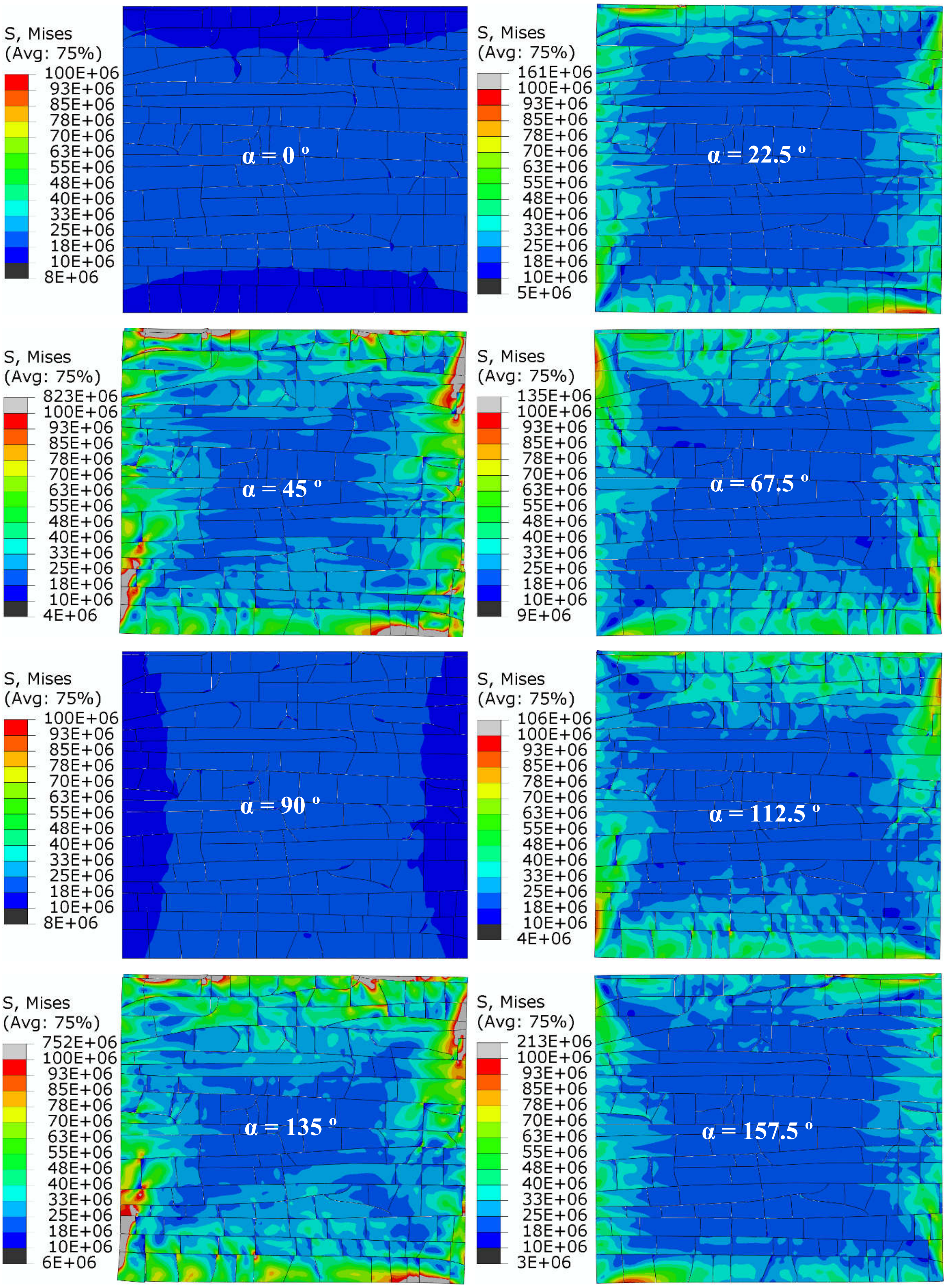
S, Mises
(Avg: 75%)
100E+06
93E+06
85E+06
78E+06
70E+06
63E+06
55E+06
48E+06
40E+06
33E+06
25E+06
18E+06
10E+06
8E+06
α = 0 º
S, Mises
(Avg: 75%)
161E+06
100E+06
93E+06
85E+06
78E+06
70E+06
63E+06
55E+06
48E+06
40E+06
33E+06
25E+06
18E+06
10E+06
5E+06
α = 22.5 º
S, Mises
(Avg: 75%)
823E+06
100E+06
93E+06
85E+06
78E+06
70E+06
63E+06
55E+06
48E+06
40E+06
33E+06
25E+06
18E+06
10E+06
4E+06
α = 45 º
S, Mises
(Avg: 75%)
135E+06
100E+06
93E+06
85E+06
78E+06
70E+06
63E+06
55E+06
48E+06
40E+06
33E+06
25E+06
18E+06
10E+06
9E+06
α = 67.5 º
S, Mises
(Avg: 75%)
100E+06
93E+06
85E+06
78E+06
70E+06
63E+06
55E+06
48E+06
40E+06
33E+06
25E+06
18E+06
10E+06
8E+06
α = 90 º
S, Mises
(Avg: 75%)
106E+06
100E+06
93E+06
85E+06
78E+06
70E+06
63E+06
55E+06
48E+06
40E+06
33E+06
25E+06
18E+06
10E+06
4E+06
α = 112.5 º
S, Mises
(Avg: 75%)
752E+06
100E+06
93E+06
85E+06
78E+06
70E+06
63E+06
55E+06
48E+06
40E+06
33E+06
25E+06
18E+06
10E+06
6E+06
α = 135 º
S, Mises
(Avg: 75%)
213E+06
100E+06
93E+06
85E+06
78E+06
70E+06
63E+06
55E+06
48E+06
40E+06
33E+06
25E+06
18E+06
10E+06
3E+06
α = 157.5 º

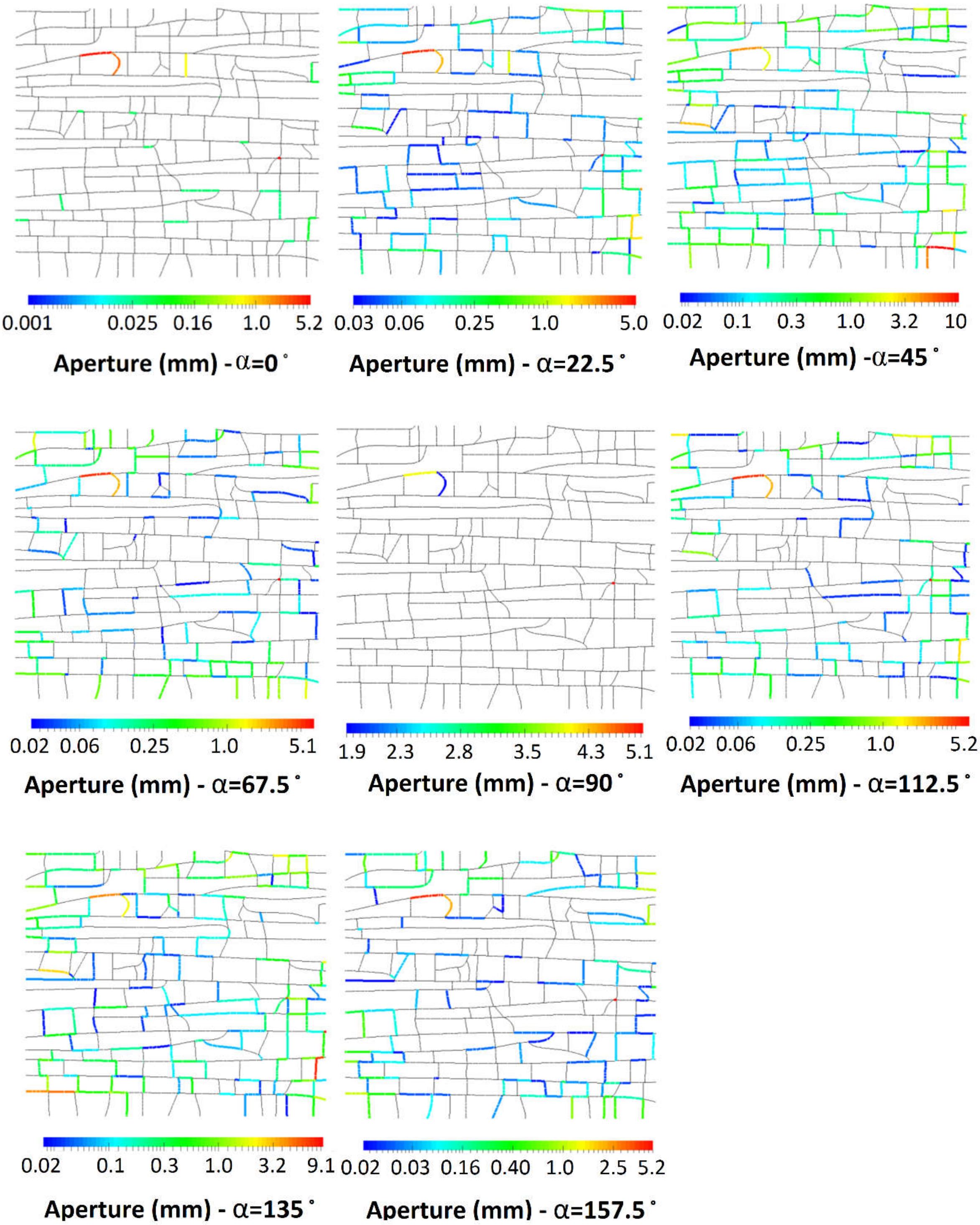
0.001 0.025 0.16 1.0 5.2
Aperture (mm) - α=0°
0.03 0.06 0.25 1.0 5.0
Aperture (mm) - α=22.5°
0.02 0.1 0.3 1.0 3.2 10
Aperture (mm) -α=45°
0.02 0.06 0.25 1.0 5.1
Aperture (mm) - α=67.5°
1.9 2.3 2.8 3.5 4.3 5.1
Aperture (mm) - α=90°
0.02 0.06 0.25 1.0 5.2
Aperture (mm) - α=112.5°
0.02 0.1 0.3 1.0 3.2 9.1
Aperture (mm) - α=135°
0.02 0.03 0.16 0.40 1.0 2.5 5.2
Aperture (mm) - α=157.5°

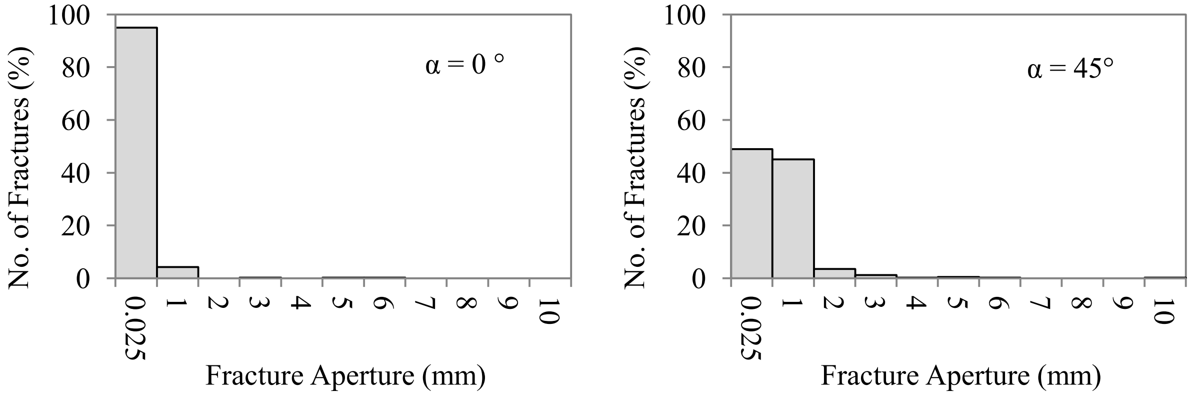

100
80
60
40
20
0
No. of Fractures (%)
α = 0 °
0.025
1
2
3
4
5
6
7
8
9
10
Fracture Aperture (mm)
α = 45°
Fracture Aperture (mm)

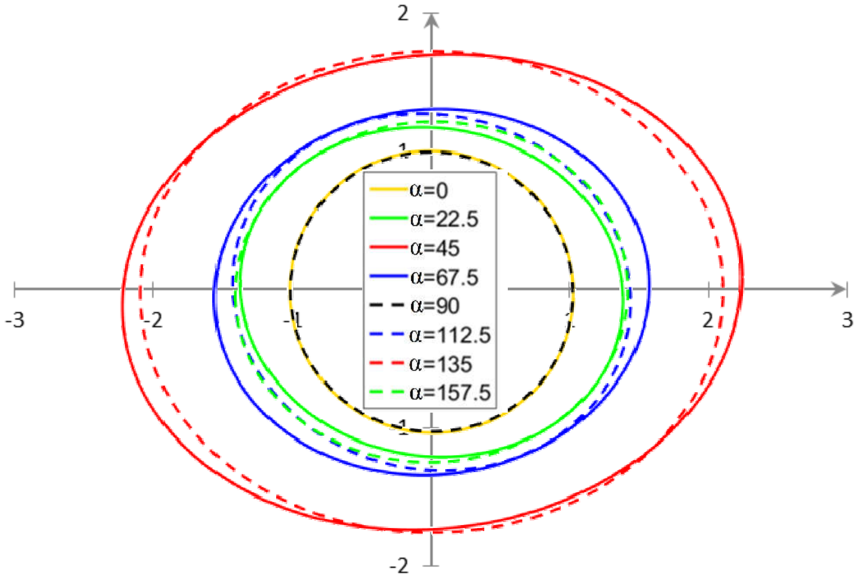

2
-3
-2
-1
1
2
3
-2
α=0
α=22.5
α=45
α=67.5
α=90
α=112.5
α=135
α=157.5

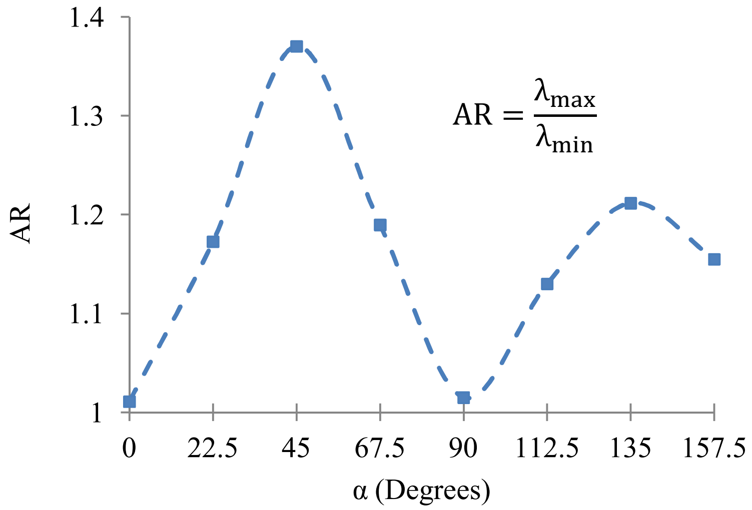
1.4
1.3
1.2
1.1
1
AR
0
22.5
45
67.5
90
112.5
135
157.5
α (Degrees)
$AR = \frac{\lambda_{max}}{\lambda_{min}}$

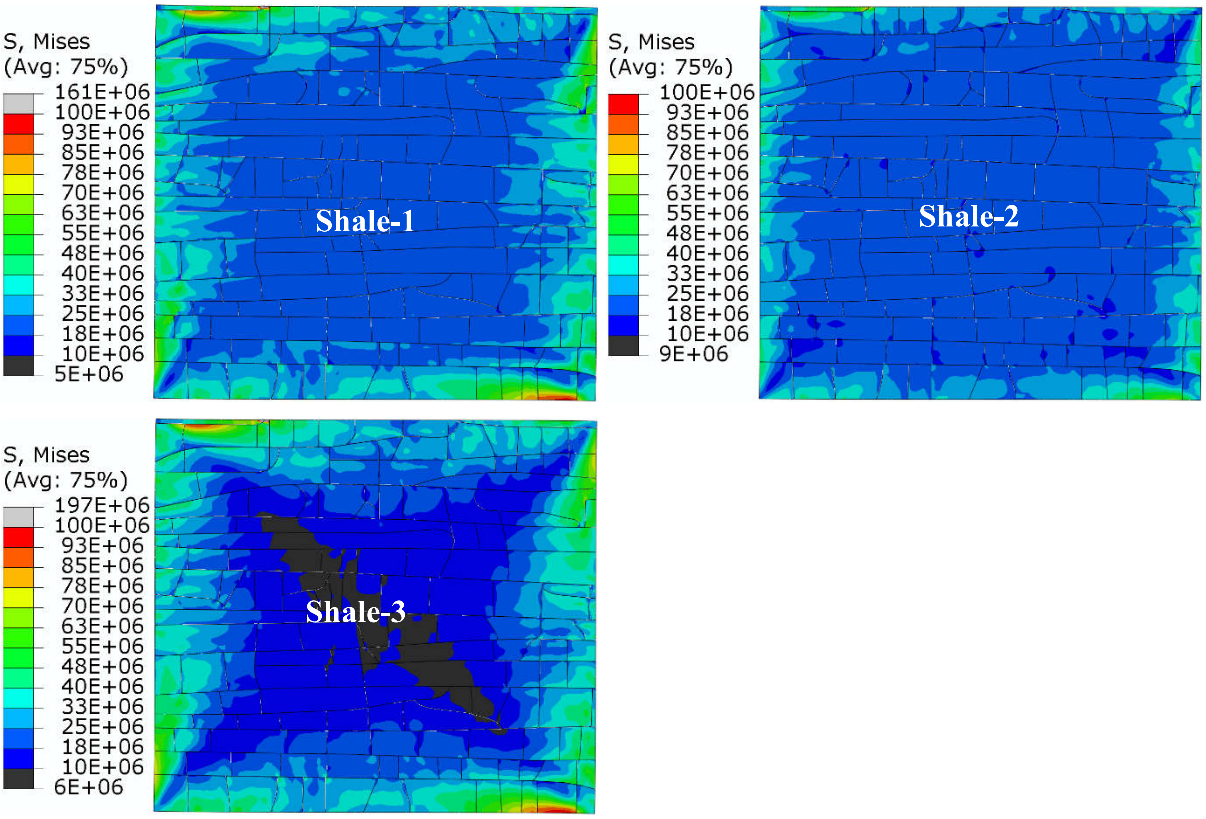
S, Mises
(Avg: 75%)
161E+06
100E+06
93E+06
85E+06
78E+06
70E+06
63E+06
55E+06
48E+06
40E+06
33E+06
25E+06
18E+06
10E+06
5E+06
Shale-1
S, Mises
(Avg: 75%)
100E+06
93E+06
85E+06
78E+06
70E+06
63E+06
55E+06
48E+06
40E+06
33E+06
25E+06
18E+06
10E+06
9E+06
Shale-2
S, Mises
(Avg: 75%)
197E+06
100E+06
93E+06
85E+06
78E+06
70E+06
63E+06
55E+06
48E+06
40E+06
33E+06
25E+06
18E+06
10E+06
6E+06
Shale-3

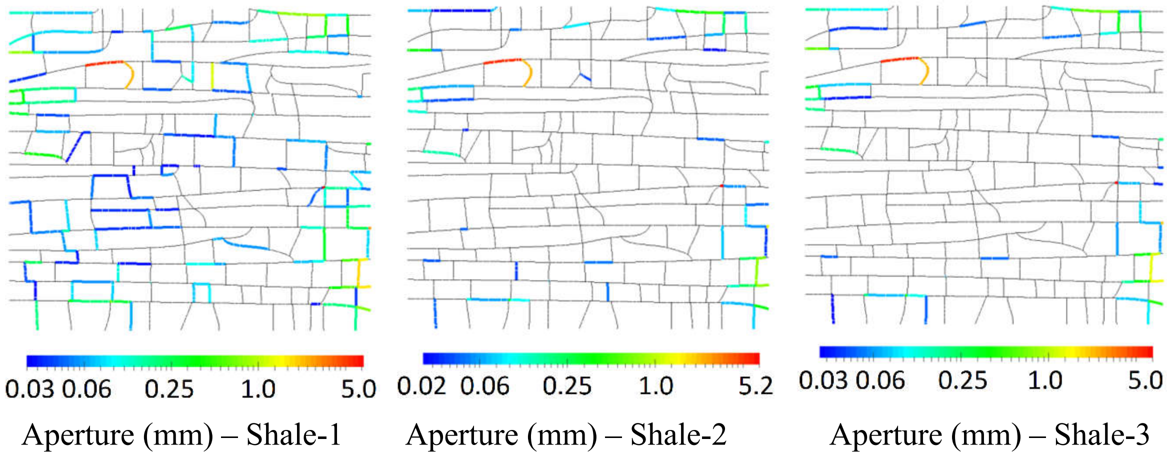
0.03 0.06 0.25 1.0 5.0
Aperture (mm) – Shale-1
0.02 0.06 0.25 1.0 5.2
Aperture (mm) – Shale-2
0.03 0.06 0.25 1.0 5.0
Aperture (mm) – Shale-3

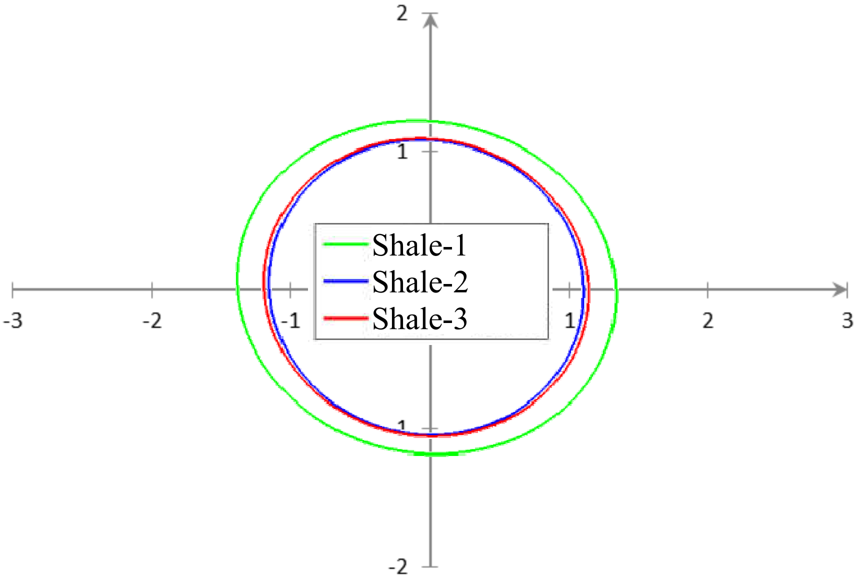
2
1
-1
-2
-3
-2
-1
1
2
3
Shale-1
Shale-2
Shale-3

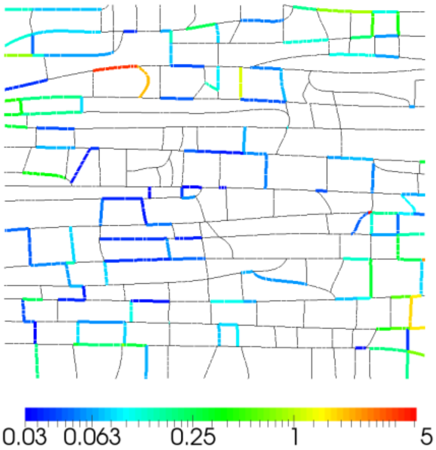

Aperture (mm) – α=22.5

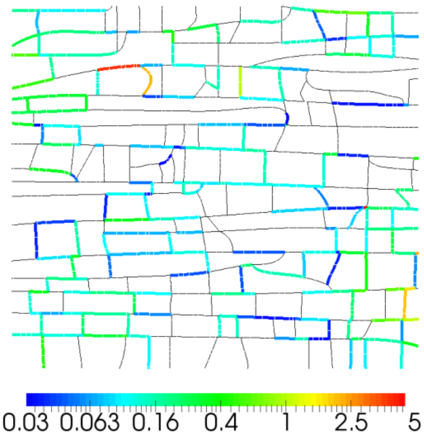

Aperture (mm) – Solid Blocks

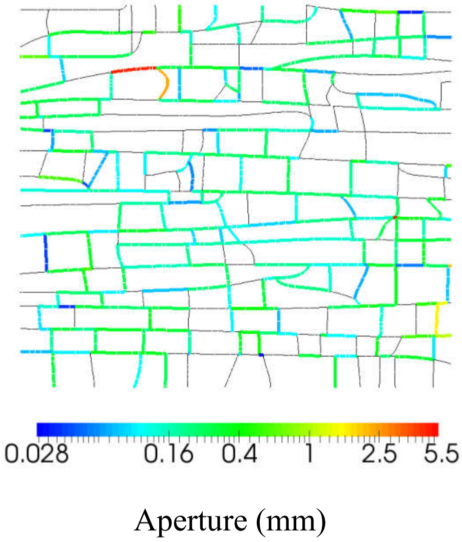
0.028
0.16
0.4
1
2.5
5.5
Aperture (mm)

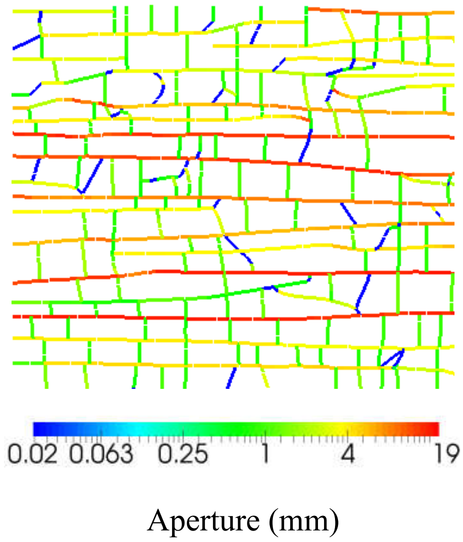
0.02
0.063
0.25
1
4
19
Aperture (mm)